Research Square

Preprints are preliminary reports that have not undergone peer review.
They should not be considered conclusive, used to inform clinical practice,
or referenced by the media as validated information.

Redox fluctuations induced the formation of hydroxyl free radicals and transformation of Fe solid phases in two paddy soils

Qiong Zhang
Zhongkai University of Agriculture and Engineering
Weihao Zhang
Zhongkai University of Agriculture and Engineering
Xiaoying Pan
Zhongkai University of Agriculture and Engineering
Jiewen Yang
jw_yang@126.com

Zhongkai University of Agriculture and Engineering

Research Article

Keywords: paddy soils, ROS, Fe phases transformation

Posted Date: March 31st, 2026

DOI: https://doi.org/10.21203/rs.3.rs-8918751/v1

License: This work is licensed under a Creative Commons Attribution 4.0 International License.
Read Full License

Additional Declarations: No competing interests reported.

Abstract

Redox fluctuation in paddy soils could lead to the formation of reactive oxygen species (ROS) as well as the Fe phases transformation, which would have great impacts on soil organic carbon (SOC) retention. However, detailed knowledge on this important geochemical process is still limited. In this study, a 11-week anoxic incubation experiment was conducted to reveal the mechanisms of ROS production by wet chemical methods and the changes in Fe phases by ^{57}Fe Mössbauer spectra (MBS) in two paddy soils (DS and XT). The results showed that significant amounts of $^{\bullet}OH$ was produced with the anoxically incubated soil slurries exposed to air oxidation. Moreover, the formation of $^{\bullet}OH$ mainly resulted from the oxygenation of surface-bound Fe(II) instead of aqueous Fe(II), and the intermediates $O_2^{\bullet-}$and H_2O_2 was confirmed to involve in the production of $^{\bullet}OH$. Due to contain more amorphous and crystalline Fe oxides, the production of Fe(II) and $^{\bullet}OH$ in DS was larger than those in XT. An alternate increase and decrease trend was observed for the $^{\bullet}OH$ production during the redox fluctuations. The MBS results showed a noticeable decrease in the content of crystalline goethite after 11-week anoxic incubation, but the content of amorphous ferrihydrite in both DS and XT kept unchanged or was increased, which resulted from the re-oxidation of Fe(II). By intensifying the oxic condition, Fe(II)-catalyzed transformation of amorphous ferrihydrite to crystalline goethite was only observed in XT, an indicative of the difference in soil mineral matrix and organic matter between the two soils. During the 11-week anoxic incubation, the concentration of dissolved organic carbon (DOC) gradually increased to its maximum at the end of 2 w, followed by a gradual decrease as anoxic incubation prolonged. This finding suggested the released DOC could be re-adsorbed onto the solid phases, possibly the newly formed amorphous ferrihydrite. The results above enhanced our understanding on the role of Fe phases in regulating the mineralization and conservation of SOC.

Introduction

Reactive oxygen species (ROS) that included hydroxyl radicals ($^{\bullet}OH$), superoxide radicals ($O_2^{\bullet-}$), and hydrogen peroxide (H_2O_2) have been found to widely participate in various soil biogeochemical processes, such as mineralization of soil carbon, attenuation of environmental pollutants (Yao et al., 2025). Recent studies have demonstrated that ROS could be produced in the dark natural redox dynamic environments like paddy soils and riparian sediments, with the mechanisms commonly ascribed to oxidation of the adsorbed and aqueous Fe(II) species coming from the reduction of iron oxides to Fe(II) induced by the redox fluctuation (Liu et al., 2024; Yang et al., 2025). Accordingly, the formation of ROS is largely related with the availability of reducible soil Fe phases and the amounts of reductant Fe(II) species (Zhao et al., 2022). It has been well recognized that the rate of this heterogeneous reduction of Fe(III) to Fe(II) is largely dependent on the crystallinity of iron oxides (Huang et al., 2021), that is, less crystalline amorphous iron oxide like ferrihydrite easily undergo reductive dissolution than those highly crystalized forms like goethite. Thus, it is reasonable to expect that the formation of ROS would vary with the availability of reducible Fe phases and the supply of Fe(II). In natural soil environments, the occurrence of phase transformation among iron oxides with different crystallinities is ubiquitous under

the circumstance of the repeated redox fluctuations, especially in paddy soils where alternative irrigation and drainage is a regular practice for rice production (Winkler et al., 2018). Up to date, knowledge on how the production of ROS is regulated by the redox fluctuation induced phase transformation of soil iron oxides was still limited.

The phase transformation of soil iron oxides driven by redox fluctuation has been well documented, whereas at present it was still hard to reach a generalized conclusion as the crystallinity of Fe-oxide could increase, decrease, or nearly keep unchanged (Cornell et al., 2003; Thompson et al., 2006; Bhattacharyya et al., 2018; Winkler et al., 2018; Chen et al., 2023). A pioneering study reported that soil redox oscillations could increase the iron-oxide crystallinity in an Inceptisol A-horizon sample in which ferrihydrite was undetectable, with the transformation of short-range ordered (SRO) minerals like nano-goethite to micro-crystalline goethite and micro-crystalline hematite (Thompson et al. 2006). Soils with contrasting difference in iron oxides composition showed different trajectories of iron oxides transformation (Winkler et al., 2018). For the soil that initially contained abundant crystalline iron oxides, the reductive dissolution could cause the depletion of crystalline iron oxides and thus decrease the iron oxide crystallinity. On the contrary, the preferential reduction of SRO iron phases coupled with leaching of aqueous Fe(II) could lead to the increase iron oxide crystallinity of the soil that was initially rich in SRO. More specifically, a 44 days duration of redox alternations imposed to a highly weathered oxisol, which initially contained 74.4% ferrihydrite and 17.6% goethite, could increase the content of goethite by nearly 9% (Bhattacharyya et al., 2018). Comparably, the continuous anoxic treatment for the same period could lead to the complete consumption of goethite, whereas goethite could be enriched under the continuous oxic treatment, with its content percentage elevated as high as 41.5%. In contrast to the previous finding detailed above, no detectable phase transformation was found for the soils enriched with high-crystallinity goethite even under the catalysis of surface-adsorbed Fe(II) (Chen et al., 2023). The contrasting discrepancy among the previous findings mainly arose from the difference in initial soil iron phase compositions, redox dynamic frequency as well as the SOC content, which block us to elucidate the underlying mechanisms on the regulation of the ROS production by the phase transformation of soil iron oxides. Hence, it raises a mechanistic question whether the formation of ROS would be inhibited or enhanced during the redox fluctuations since this kind of redox dynamic could change the content of reducible iron phases.

Under the ambient conditions, the transformation of thermodynamically unstable ferrihydrite to more crystalline iron oxides like goethite and hematite has been widely observed, which proceeded via two pathways: (i) dissolution-recrystallization (also called Ostwald ripening) and (ii) catalysis of surface adsorbed Fe(II) (Cornell et al., 2003). As for the pathway (i), Fe(II) was released to solution due to the dissolution of ferrihydrite, which could eventually reprecipitate into goethite through a nucleation-crystal growth process, with the incorporation among the monovalent forms of $Fe(OH)^{2+}$ at the acidic pH or $Fe(OH)_4^-$ at neutral and basic pH (Burleson et al., 2006). The second pathway involved the electron transfer between the surface adsorbed Fe(II) and structural Fe(III), and the subsequent formation of surface labile Fe(III) that was the ideal seeds and key intermediates for the growth of goethite crystal

(Sheng et al., 2020; Liu et al., 2022). However, such transformation was always observed in those pure reaction systems, which was always limited in real soil environments. For example, the presence of OM could completely inhibit the Fe(II)-catalyzed transformation of ferrihydrite or facilitate the formation of lepidocrocite instead of more crystalline goethite, which is largely dependent on the its content and type (Chen et al., 2015; Zhou et al., 2018). It is indeed that iron hydroxides always existed with SOC as the form of coherent mixtures in natural soils. Therefore, the contradicts among the previous studies about the Fe phases transformation induced by redox fluctuation brought us to hypothesize that the production of ROS might be enhanced with the re-oxidation of aqueous Fe to the reducible iron phases again. Otherwise, it would be decreased with the increase in crystallinity of Fe phases.

Given the considerations above, two paddy soils that were different in the content of Fe phases and content of OM were used in this study to examine the redox fluctuations induced formation of ROS, and the emphasis was put on revealing how the production of $^{\bullet}OH$ was regulated by the transformation between reducible Fe phases and those less reactive. Mössbauer spectroscopy (MBS) were adopted to decipher the changes in iron oxide species under redox fluctuations. The results herein would further improve our understanding on the coupling of iron redox cycles and the formation of ROS under natural conditions together with the biogeochemical cycle of associated elements like C.

Materials and methods

Chemicals and Soil Samples.

The two paddy soil samples used in this study were collected from the 0 - 20 cm surface horizon of paddy fields in Guangdong Province, China. One sampling site (23.714297 °N, 113.264525 °E) was located at Dushu Village, Qingcheng District, Qingyuan (DS), and the other (23.238386°N, 112.320818 °E) was located at Xutou Village, Gaoyao District, Zhaoqing (XT). The soils were air-dried and ground to pass through 2 mm mesh-size sieve. The related physicochemical properties of the soils were analyzed according to the published methods (Sparks, 1996), with the results presented in Table S1.

Incubation Experiments

All experiments were conducted in triplicate in the dark at room temperature. Soil reaction systems for determination of ROS were separately prepared from those for analyzing aqueous Fe, pH, DOC and solid Fe phases with the same methods. Initially, 5.0 g of soil (oven dry weight) was weighed into a 50 mL plastic centrifuge tube, followed by addition of 25 mL distilled water with removal of dissolved O_2 by boiling. The tubes were tightly wrapped with parafilm and then capped with airtight lids to rule out the interference of O_2 from air with the establishment of anoxic incubation. The anoxic incubation lasted for 11 w, with the tubes periodically shaken by hand to mix suspensions. At the end of anoxic incubation experiments, the tube was centrifuged, and the supernatant was collected for Fourier transform ion cyclotron resonance mass spectrometry (FT-ICR MS) analysis. The pellets were freeze-dried, and stored in refrigerator for MBS analysis. Moreover, to assess the Fe phases transformation under oxic condition,

the soil slurry was anoxically incubated in tube for 4 w, which was subsequently bubbled with O_2 for 1 d and exposed to air for 1 w. The soil samples used for MBS analysis were collected with the same methods as detailed above.

Analysis Methods

Determination of ˙OH. At specific time intervals of anoxic incubation experiments, a tube was sacrificed to investigate the production of ˙OH. Hydroxylation reaction between benzoic acid (BA) and ˙OH was used to quantify the concentration of ˙OH by measuring the formation of *p*-hydroxybenzoic acid (*p*-HBA). Firstly, a required volume of capturing agent BA to the suspensions by carefully penetrating the parafilm with a fine stainless syringe needle. Subsequently, the parafilm was removed to allow the suspensions exposed to air to initiate the production of ˙OH resulting from the oxygenation of Fe(II). After exposure to air for 8 h, 0.5 mL suspension samples were withdrawn into a 1.5 mL centrifuge tube, followed by adding 0.5 mL methyl alcohol to quench the hydroxylation reaction. The tube was centrifuged at 12 000 rpm for 5 min, and the supernatant was passed through 0.22 μm for HPLC analysis of *p*-HBA. The concentration of *p*-HBA was measured by an Agilent 1260 Infinity II HPLC system equipped with a ThermoFisher Scientific reverse-phase C 18 column (150 × 4.6 mm, 5 μm, Hypersil GOLD™) and a UV-detector. The mobile phase was a mixture of methyl alcohol and 0.1% acetic acid (30:70, v/v) at a flow rate of 1 mL min^{-1}, with the injection volume of 10 µL. The column temperature was controlled at 35°C, and the detection wavelength was set at 255 nm. To find out the formation mechanism of ˙OH, nitro blue tetrazolium chloride (NBT) and bovine liver catalase (CAT) were used to quench $O_2^{\bullet-}$ and H_2O_2, respectively. According to the formation yield of the hydroxylation product, the ˙OH concentration was calculated based on the *p*-HBA concentration with the conversion factor of 5.87.

To investigate the effect of newly formed surface Fe(III) forms on the production of ˙OH, the soil slurry was anoxically incubated in tube for 1 or 2 w, and then bubbled with O_2 for 1 d to accelerate the oxidation of the previously produced Fe(II) and the subsequent formation of fresh surface Fe(III) forms. Afterwards, the soil slurries were anoxically incubated for 1 w, and the production of ˙OH was investigated according to the abovementioned procedures. For brief description, the incubation experiments above were named as R1 (1 w anoxic incubation, 1 d bubbling with O_2 and 1 w anoxic incubation) and R2 (2 w anoxic incubation, 1 d bubbling with O_2 and 1 w anoxic incubation), respectively.

Determination of Fe(II) and H_2O_2. Samples for analysis of Fe(II) and H_2O_2 were collected from another separate batch of reaction systems prepared with the methods identical to those for ˙OH. When determining Fe(II) at each sampling, the lids of tubes were removed while the parafilm was still left to avoid the inadvertent oxygenation by air. An appropriate volume of supernatant was sampled with a fine stainless syringe needle by penetrating the parafilm, followed by filtration into a vial containing color-developing reagent. The concentration of Fe(II) was measured by the 1,10-*o*-phenanthroline analytical method at 510 nm using a UV-visible spectrophotometer with the detection limit of 0.1 mg L^{-1}. As for

determination of H_2O_2, 5 mL of supernatant was taken out and filtered into the sample bottle. The concentration of H_2O_2 was measured according to the horseradish peroxidase (POD) catalyzed oxidation of N, N-diethyl-p-phenylenediamine (DPD) by H_2O_2 (Hsieh et al., 2014). In brief, 2 mL phosphate buffer (0.5 M, pH = 6.0), 50 μL of DPD solution (10 mg L^{-1}) and 50 μL of POD solution (1 mg L^{-1}) were consecutively added to the sample solution, and the working was diluted to 10 mL with deionized water. The concentration of H_2O_2 was obtained by comparing the absorbance at 551 nm with that of standard solutions. After completion of sampling for the determination of aqueous Fe(II) and H_2O_2 as described above, an aliquot volume of trace-metal-grade HCl was added to make the volume of suspensions back to 25 mL with the concentration of HCl kept at 0.5 M to extract surface-bound Fe(II). After mixing for 2 h at 180 r min^{-1}, the tube was centrifuged at 4000 rpm for 10 min for the determination of total aqueous Fe(II). The surface-bound Fe(II) was obtained by subtracting aqueous Fe(II) from total Fe(II).

^{57}Fe Mössbauer Measurement. ^{57}Fe Mössbauer spectra were recorded on a WSS-10 spectrometer controlled by Wissoft 2003. The JANIS Cryostat SHI-850-5 was used for temperature control at 6 K in constant acceleration mode, with a ^{57}Co (Rh) used as the gamma energy source. MossWinn 4.0 was used for the quantitative evaluation of the spectral parameters (least-squares fitting to Lorentzian peaks). The minimum experimental line widths were 0.27 mm·s-1. The temperature of the samples was controlled by a LakeShore Modle 335 within an accuracy of ± 0.3 K. All center shifts (CSs) and peak positions were calibrated relative to α-iron at 298 K.

Molecular characterization of DOC by FT ICR-MS. All samples were extracted via solid-phase extraction (SPE) to desalinate and concentrate before FT ICR-MS analysis by use of Agilent Bond Elut® PPL cartridges (1 g mL^{-1}). The column was activated by rinsing 6 mL of MS grade methanol prior to use. 15-30 mL of samples that had been acidified to pH 2.0 with 32% analytical grade HCl was dropwise passed through the column, followed by sequentially rinsing the columns with two cartridge volumes of 0.01 M HCl and two cartridge volumes of ultra-pure water to remove residual salts. Afterwards, the column was dried under N_2 air flow, and was immediately extracted with two column volumes of MS grade methanol. The methanol eluent samples were blown dried with N_2, and stored in the dark at -20 °C. An appropriate amount of dried sample was withdrawn for FT-ICR MS analysis, which was dissolved in approximately 2 mL of 50:50 methanol/water (v/v) with the concentration of total organic carbon (TOC) maintained below100 mg L^{-1}.

A Bruker solariX XR FT-ICR mass spectrometer (Bruker Daltonik GmbH, Bremen, Germany), equipped with a 9.4 T refrigerated actively shielded superconducting magnet (Bruker Biospin, Wissembourg, France) and an ESI ion source under negative ion mode (Bruker Daltonik GmbH, Bremen, Germany), was used to perform ultrahigh resolution mass spectrometry analysis of DOC samples. For each spectrum, a total of 128 continuous 4 M data FT-ICR transients were co-added to enhance the signal-to-noise ratio and dynamic range, with mass range m/z 150 to 800 Da and ion accumulation time of 0.02 s. A list of known formula mass peaks was used as external calibration of the mass spectra, with the final spectrum internally recalibrated with typical O_2 class species peaks by using quadratic calibration in

DataAnalysis 5.0 (Bruker Daltonics). A typical mass-resolving power (m/Δm50%, in which Δm 50% is the magnitude of the mass spectral peak full width at half-maximum peak height) > 450 000 at m/z of 319 with < 0.3 ppm absolute mass error was achieved. Custom software was used to calculate all mathematically possible formulas for all ions with a signal-to-noise ratio (S/N) > 4 and a mass error < 0.5 ppm.

The maximum number of atoms in the formula calculator was set to 30 ^{12}C, 60 ^{1}H, 20 ^{16}O, 3 ^{14}N, 1 ^{32}S, 1 ^{13}C, 1 ^{18}O and 1 ^{34}S. The identified formulas containing isotopomers (e.g., ^{13}C, ^{18}O and ^{34}S) are not discussed. For the chemical formula of $C_cH_hO_oN_nS_s$, the double bond equivalence (DBE) is calculated according to the following equation: DBE= 1 + (2c - h + n)/2, where c, h, and n are the numbers of carbon, hydrogen, and nitrogen atoms, respectively. The details of data processing and the methods for calculating the aromaticity index (AI) that was adopted to measure the aromaticity of each compound have been described by previous studies (Koch & Dittmar 2006; Jiang et al., 2014). The parameters, H/C ratio and O/C ratio, were used for constructing van Krevelen diagram.

Statistical Analysis

All experiments were conducted in triplicate, and results were expressed as the mean ± standard deviation (SD).

Results and discussion

Production of Fe(II) and ˙OH during the anoxic incubation.

The Fe(II) produced during the anoxic incubation mainly existed on the soil solid surfaces, which was due to the relatively high pH value of reaction systems. Generally, the pH of reaction system was above 6.0 during the initial 6-w anoxic incubation period (Fig. S1), but it gradually decreased as the incubation prolonged to 11 w. This pH condition would lead to the soil surfaces more negatively charged, and then was favorable for the electrostatic attraction between the surface and cationic Fe(II) (Zhu et al., 2014; Tomaszewski et al., 2016). Therefore, the Fe(II) produced during the anoxic incubation mainly existed as surface-bound forms. As shown in Fig. S2, the concentration of dissolved Fe(II) in DS could reach to 66.79 μM after anoxic incubation for 1 w, which decreased to 35.46 μM at the end of 2 w and became undetectable thereafter. Similarly, the aqueous Fe(II) in XT was as low as 20.06 μM at the end of 1-w anoxic incubation and was not measured as incubation continued.

By contrast, significant amounts of surface-bound Fe(II) that was extracted by 0.5 M HCl were detected in the two soils during the whole anoxic incubation period, with its concentration ranging from 1.94 to 5.15 g kg^{-1} and 0.77 to 2.84 g kg^{-1} for DS and XT, respectively (Fig. 1a). Meanwhile, both the soils displayed the same trend for the changes in the concentration of surface-bound Fe(II) over the whole incubation period, reaching its peak at the end of 2 w and gradually decreased as the experiments continued. This trend suggested that the reducible Fe component was gradually consumed. Moreover,

the production of Fe(II) in DS was significantly higher than that in XT, which indicated the great difference in the availability of reducible iron phases (electron acceptors), the availability of electron donors and the activities of microbial Fe reducers between the two paddy soils.

Once the anoxic incubation systems were exposed to air-oxidation, production of $^{\bullet}OH$ was detected throughout the whole experiment. It was shown in Fig. 1b that the concentration of $^{\bullet}OH$ in DS ranged from 8.21 to 20.85 μM and from 6.54 to 11.64 μM in XT. The production of $^{\bullet}OH$ in DS was also larger than that in XT at most sampling times, which was similar to the trend observed for the generation of Fe(II) as shown in Fig. 1a. This similarity indicated that there was a close relationship between the production of $^{\bullet}OH$ and Fe(II). More importantly, an alternate increase and decrease pattern of $^{\bullet}OH$ production was observed with the redox fluctuations instead of continuous increase or decrease, which was an indicative of the transformation of Fe phases caused by the redox fluctuations, specifically the oscillation in the content of reducible Fe phases. During anoxic periods, the adsorption of the aqueous Fe(II) ions to Fe mineral surfaces has been shown to accelerate the transformation of ferrihydrite to well-ordered Fe phases like goethite that are less chemically reactive and bioavailable than ferrihydrite (Hansel et al., 2003; Chen et al., 2018). Therefore, the original reducible Fe phases like ferrihydrite were consumed with the rapid generation of Fe(II), which could lead to the continuous increase in the production of $^{\bullet}OH$ during the initial stage of anoxic incubation (Fig. 1b). With the depletion of original reducible Fe phases as well as the transformation of ferrihydrite to well-ordered Fe phases like goethite, the re-supply of reducible Fe phases was limited, which thus constrained the generation of Fe(II) and the subsequent production of $^{\bullet}OH$.

To further explore the transformation of Fe phases on the production of $^{\bullet}OH$, the soils were further treated with two different intensities of redox fluctuation cycles (R1 and R2). During the 1 or 2 w anoxic incubation, the reducible Fe phases was rapidly consumed with the release of Fe(II) (Fig. 1a). When exposing to the bubbled O_2, oxidation of those produced Fe(II) together with the transformation of Fe phases occurred, which thus impacts the production of $^{\bullet}OH$. It was shown in Fig. S3 that significant production of Fe(II) and $^{\bullet}OH$ was still detected at the end of each examined redox fluctuation cycle. However, the production of both Fe(II) and $^{\bullet}OH$ at the end of R1 was more than those measured for R2 for both DS and XT. Clearly, this result indicated crystallinity of Fe oxides was more increased during redox fluctuation cycle R2, with the decrease in the content of reducible Fe phases. Therefore, the decrease in the production of $^{\bullet}OH$ as shown in Fig. S3 was detected. Redox fluctuations or continuous oxic incubation has been confirmed to increase the crystallinity of soi Fe oxides (Chen et al., 2018).

In order to reveal the pathways of $^{\bullet}OH$ production, chemical analysis and quenching experiments were performed to probe the generation of intermediates like $O_2^{\bullet-}$ and H_2O_2. Collectively, there were four successive steps likely involved in the pathways for the production of $^{\bullet}OH$. Under anoxic conditions, the soil surface-bound Fe(III) was abiotically or biotically reduced to Fe(II). When shifted to aerobic conditions, surface-bound Fe(II) reacted with O_2 to form $O_2^{\bullet-}$, followed by the subsequent formation of

H_2O_2 resulting from the reaction between the additional surface-bound Fe(II) and $O_2^{\bullet-}$. Finally, the reaction between additional surface-bound Fe(II) and H_2O_2 led to the formation of $^{\bullet}OH$. The pathways for the production of $^{\bullet}OH$ could be expressed as the equations below.

Surface-bound Fe(III) + e^- + H^+ → Surface-bound Fe(II) + H_2O (1)

Surface-bound Fe(II) + O_2 → Surface-bound Fe(III) + $O_2^{\bullet-}$ (2)

Surface-bound Fe(II) + $O_2^{\bullet-}$ + 2H^+ → Surface-bound Fe(III) + H_2O_2 (3)

Surface-bound Fe(II) + H_2O_2 → Surface-bound Fe(III) + $^{\bullet}OH$ + OH^- (4)

A reaction system that experienced anoxic incubation for 5 w was selected as an example to probe the generation of intermediates above. Quenching experiment was performed to confirm the participation of H_2O_2 and $O_2^{\bullet-}$ in the production of $^{\bullet}OH$. With the addition of CAT (960 U mL^{-1}), the typical scavenger of H_2O_2, the production of $^{\bullet}OH$ in DS and XT was decreased by 18.3% and 17.5%, respectively (Fig. 2a). Similarly, the addition of 1.0 mM NBT, the quencher of $O_2^{\bullet-}$, could decrease the production of $^{\bullet}OH$ by 17.5% and 15.7%, respectively.

Additionally, the existence of $O_2^{\bullet-}$ was also verified by use of the formation of XTT formazan from XTT. As shown in Fig. 2b, the formation of XTT formazan was observed as a characteristic UV absorption peak at 475 nm was detected, which was consistent with that reported in previous studies.[4] Moreover, H_2O_2 could be directly detected in the aqueous phases of DS at the end of each redox fluctuation treatment during first two weeks with its concentration ranging from 66.25 to 80.83 μM (Fig. S2), which was in contrast to the fact that H_2O_2 could only be measured in the XT solutions at the end of the first week with its concentration of 47.50 μM. This phenomenon was in agreement with that observed for the dissolved Fe(II) (Fig. 1a), indicating that the production of $^{\bullet}OH$ partly occurred in aqueous phases of DS but mainly came from the soil solid-liquid interface as the experiments prolonged.

Transformation of soil Fe phases.

Mössbauer spectroscopy (MBS) was used to analyze the changes in Fe solid phases with data modeling at 6 K. The fitting results with the Fe solid phases assignment were given in Table S2, where averaged values for center shift (CS), quadrupole splitting (QS) and hyperfine magnetic field (H) are reported. The MBS collected at 6 K from the original and the treated soils commonly showed a typical doublet (D1) (Fig. 3), with the fitting parameters in agreement with those of solid-associated Fe(II) (Q-Fe(II)) existing in primary/secondary minerals or as the silicate-associated or adsorbed forms (Mikutta et al., 2024). Generally, Q-Fe(II) doublet is a minor component of the spectra of all the original and treated soil samples. As shown in Table S2, Q-Fe(II) only accounted for 6.36% of spectral area of the original DS, 7.66% after 11 w anoxic incubation, and 9.47% after 4 w anoxic -1 w oxic incubation. For the original XT,

the percentage of spectral area represented by Q-Fe(II) was 11.10%, which was 16.04% after the soil sample treated with 11-w anoxic incubation and 11.66% after 4-w anoxic -1-w oxic incubation. This slight increase in the content of Q-Fe(II) component mainly resulted from the accumulation of Fe(II) produced during the reductive dissolution of Fe (oxy)oxides onto the soil surfaces.

Since Fe atoms in monomeric Fe(III)-organic complexes and Fe(III)-silicates (Q-Fe(III)) were too distant from each other to order magnetically, another doublet (D2) was also observed for all the examined soil samples (Fig. 3), which was the characteristic MBS of Fe(III) in these components. For all the samples, the MBS CS values of these components at 5 K ranged from 0.40 - 0.49 mm s^{-1}, but the quadrupole splitting (QS) values that were more variable (0.66-0.87 mm s^{-1}). It was reported that Fe(III)-substituted phyllosilicate minerals commonly yield QS values in this range, with a QS value of 0.5 mm s^{-1} for Fe-substituted kaolinite and QS values of ~0.8 mm s^{-1} for 2:1 layer clays yielding or higher for Fe-poor 2:1 minerals (Murad & Wagner, 1994; Murad, 1998). It was worthwhile to note that organic-complexed Fe(III) can also yield doublets with parameters similar to those Fe(III) in silicates. Therefore, it is difficult to use MBS to distinguish organic-complexed Fe(III) from Fe(III) in silicates. As shown in Table S2, the content of Q-Fe(III) in the original DS was 20.7%, which was slightly increased to 25.8% after 11 w anoxic incubation (24.3% relative change) and to 23.05% after 4 w anoxic - 1 w oxic incubation (11.3% relative change). Since the Fe(III)-substitution in phyllosilicate minerals was unlikely to occur under the present reaction systems, the increase in the content of Q-Fe(III) could be attributed to the newly released Fe(III) during the reductive dissolution binding to the surface organic substances. Relatively, a reverse trend was observed for change in the content of Q-Fe(III) in XT as the content of this component decreased from 32.4% to 24.49% after 11-w anoxic incubation (-24.4% relative change) and to 27.15% after 4-w anoxic and 1-w oxic incubation (-16.2% relative change). The contrasting changes in the content of both Q-Fe(III) and Q-Fe(II) between DS and XT were determined by different physicochemical factors included in the two soil reaction systems like content of SOC, rate of Fe(II)-catalyzed ferrihydrite transformation and effect of mineral matrix templating (Zhou et al., 2018; Liu et al., 2025), which also controlled the changes for the contents of Fe(III)-(oxy)hydroxides (Fe(III)-OxHy) and Fe(III) oxides (Fe(III)-Ox) as addressed below.

In addition to doublet, two broadened sextets appeared in the MBS of all the soil samples at 6 K (Fig. 3). As given in Table S2, the sextet with a small hyperfine field (~ 45 T) was assigned to the component of poorly crystallized Fe(III)- OxHy like amorphous ferrihydrite, and the sextet with a large hyperfine field (~ 49 T) corresponded to the fraction of well crystallized Fe(III)-Ox like goethite. The identification of solid Fe phases with sextets in this study was in agreement with that reported by previous studies (Thompson et al., 2011; Giannetta et al., 2022). For DS, it originally contained 19.44% of Fe(III)-OxHy, and no change was found for the content of this component after either 11-w anoxic incubation or 4-w anoxic – 1-w oxic incubation. In contrast, the content of Fe(III)-Ox was decreased from 53.49% to 47.22% after 11-w anoxic incubation (11.7% relative change) and to 47.87% after 4-w anoxic – 1-w oxic incubation (10.5% relative change) (Table S2 and Fig. 4a). The preferential ligand/reductive-promoted dissolution of ferrihydrite over more crystalline Fe oxides has been widely acknowledged (Huang et al., 2021). From the

perspective of mass balance of Fe(III), the reason for no change in the content of Fe(III)- OxHy could be tentatively attributed to the re-precipitation of aqueous Fe(III) to ferrihydrite on the soil surfaces, which thus replenished the loss of initial Fe(III)-OxHy during the initial reductive dissolution stage. Compared to DS, significant changes were found for the content of Fe(III)-OxHy and Fe(III)-Ox in XT after the same treatments. As shown in Table S2 and Fig. 4b, 11-w anoxic incubation resulted in a large increase in the percentage of Fe(III)-OxHy from 16.46% to 41.07%, which coincided with a decrease in the content of Fe(III)-Ox from 40.03% to 18.4%. Once again, this result confirmed the occurrence of the re-precipitation of aqueous Fe(III) to ferrihydrite on the soil surfaces as stated for the DS reaction systems above. The extremely limited supply of dissolved O_2 in this treatment significantly blocked the Fe(II)-catalyzed transformation of ferrihydrite to goethite (Hansel et al., 2003). In contrast, 4-w anoxic – 1-w oxic incubation led to a large decrease of the content of Fe(III)-OxHy from 16.46% to 8.25% and a remarkable increase of the content of Fe(III)-Ox from 40.03% to 52.95% (Table S2 and Fig. 4b). It was evident that the supply of dissolved O_2 in this treatment promoted the Fe(II)-catalyzed transformation of ferrihydrite to goethite (Chen et al., 2018). Since the mineral matrix as well as the content and type of SOC had critical impact on this process (Zhou et al., 2018; Liu et al., 2025), no occurrence of Fe(II)-catalyzed transformation of ferrihydrite to goethite in DS was indicative of the difference in physicochemical properties between the two soils (Table S1). Soil SOC has been demonstrated to hinder the electron exchange between adsorbed Fe(II) and Fe(III) in minerals and then decrease the extent of Fe minerals transformation in soils (Chen et al., 2023).

Release of SOC during anoxic incubation

The concentration of DOC during the 11-w anoxic incubation was also simultaneously monitored with its molecular composition analyzed by FT-ICR MS. As shown in Fig. 5, both DS and XT exhibited the same trend for the changes in the concentration of DOC, which reached its maximum at the end of 2 w (21.02 mg L^{-1} for DS) or 3 w (20.6 mg L^{-1} for XT) and then gradually decreased across the following period. This trend could indicate a close association between the release of SOC and the reductive dissolution of Fe phases, and, more importantly, a mineral-associated SOC protection mechanism in paddy soils (Chen et al., 2014; Huang et al., 2017). In this mechanism, the reductive dissolution of Fe phases could lead to the release of SOC into aqueous solution during the initial stage. However, SOC would be bound by the soil surfaces again during the following stage due to the formation of co-precipitates between Fe(II/III) cations and DOC as well as the re-adsorption of DOC onto the newly formed iron (hydro)oxides. As confirmed by our MBS results (Fig. 4b), amorphous ferrihydrite was regenerated, which possesses a large surface area and a high affinity for SOC (Huang et al., 2017).

The molecular compositions of DOC were further analyzed by use of FT-ICR MS. As illustrated in Table S3, three classes of CHO, N-containing (including CHON and CHONS), and CHOS formulas typically represented the highest abundance fraction in all DOC molecules, with 77.89% for DS and 74.39% for XT. According to the ratio of H/C and O/C of each molecular formula, DOC molecules are classified into seven categories that included lipids (O/C = 0~0.3; H/C 1.5~2), proteins (O/C: 0.3~0.67; H/C 1.5~2.2), carbohydrates (O/C: 0.67~1.2; H/C 1.5~2.4), unsaturated hydrocarbon (O/C: 0~0.1; H/C 0.5~1.5), lignin-

like (O/C: 0.1~0.67; H/C 0.7~1.5), tannins (O/C: 0.67~1.2; H/C 0.5~1.5), and condensed aromatics (O/C: 0~0.67; H/C 0.2~0.7) (Table 1). The distribution of DOC molecular compositions was visualized with van Krevelen (Fig. 6). For both DS and XT, lignin-like, tannins, and condensed aromatics accounted for more than 80% of the composition of DOC, which were believed to be resistant to microbial decomposition. Additionally, the reductive capacity of DOC in DS was higher than that of XT as it owned more negative NOSC value and higher DBE-O value (Table S3).

Declarations

Author Contributions

Qiong Zhang: Conceptualization, Methodology, Formal analysis, Writing-original draft; Weihao Zhang: Methodology, Operation and completion of the experiment, Data Processing; Xiaoying Pan: Conceptualization, Writing-original draft; Jiewen Yang: Conceptualization, Funding Acquisition, Resources, Supervision, Writing-Review & Editing.

Funding This study was supported by the National Natural Science Foundation of China (42471075) and Guangdong Province Key Field Research and Development Program (2023B0202010027).

Data Availability Data will be made available upon request.

Ethics Approval The authors declare that this study does not involve animals.

Consent for Publication All the authors approved the manuscript for publication.

Competing Interest The authors declare that they have no known competing financial interests or personal relationships that could have appeared to influence the work reported in this paper.

References

1. Bhattacharyya, A., Campbell, A. N., Tfaily, M. M., Lin, Y., Silver, W. L., Nico, P. S., & Pett-Ridge, J. (2018). Redox fluctuations control the coupled cycling of iron and carbon in tropical forest soils. Environmental Science & Technology, 52(24), 14129–12139. https://doi.org/10.1021/acs.est.8b03408
2. Burleson, D. J., & Penn, R. L. (2006). Two-step growth of goethite from ferrihydrite. Langmuir, 22, (1), 402-409. https://doi.org/10.1021/la051883g
3. Chen, C., Kukkadapu, R., & Sparks, D. L. (2015). Influence of coprecipitated organic matter on $Fe^{2+}_{(aq)}$ - catalyzed transformation of ferrihydrite: implications for carbon dynamics. Environmental Science & Technology, 49(18), 10927– 10936. https://doi.org/10.1021/acs.est.5b02448
4. Chen, C. M., Dong, Y. J., & Thompson, A. (2023). Electron transfer, atom exchange, and transformation of iron minerals in soils: the influence of soil organic matter. Environmental Science & Technology, 57(29), 10696-10707. https://doi.org/10.1021/acs.est.3c01876

5. Chen, C. M., Dynes, J. J., Wang, J., & Sparks, D. L. (2014). Properties of Fe-organic matter associations via coprecipitation versus adsorption. Environmental Science & Technology, 48(23), 13751-13759. https://doi.org/10.1021/es503669u
6. Chen, C. M, Meile, C., Wilmoth, J., Barcellos, D., & Thompson, A. (2018). Influence of pO_2 on iron redox cycling and anaerobic organic carbon mineralization in a humid tropical forest soil. Environmental Science & Technology, 52(), 7709-7719. https://doi.org/10.1021/acs.est.8b01368
7. Cornell, R. M., & Schwertmann, U. (2003). Transformations. In R. M. Cornell, & U. Schwertmann (Eds.), The iron oxides: structure, properties, reactions, occurrences and uses (2nd ed., pp 365-408). Wiley-VCH: Weinheim, Germany.
8. Giannetta, B., Plaza, C., Thompson, A., Pkante, A. F., & Zaccone, C. (2022). Iron speciation in soil size fractions under different land uses. Geoderma, 418, 115842. https://doi.org/10.1016/j.geoderma.2022.115842
9. Hansel, C. M., Benner, S. G., Neiss, J., Dohnalkova, A., Kukkadapu, R. K., & Fendorf, S. (2003). Secondary mineralization pathways induced by dissimilatory iron reduction of ferrihydrite under advective flow. Geochimica et Cosmochimica Acta, 67(16), 2977-2992. https://doi.org/10.1016/S0016-7037(03)00276-X
10. Huang, J. Z., Jones, A., Waite, T. D., Chen, Y. L., Huang, X. P., Rosso, K. M., Kappler, A., Mansor, M., Tratnyek, P. G., & Zhang, H. C. (2021). Fe(II) redox chemistry in the environment. Chemical Reviews, 121(13), 8161–8233. https://doi.org/10.1021/acs.chemrev.0c01286
11. Hsieh, H. S., Wu, R. R., & Jafvert, C. T. (2014). Light-independent reactive oxygen species (ROS) formation through electron transfer from carboxylated single-walled carbon nanotubes in water. Environmental Science & Technology, 48(19), 11330–11336. https://doi.org/10.1021/es503163w
12. Huang, W., & Hall, S. J. (2017). Elevated moisture stimulates carbon loss from mineral soils by releasing protected organic matter. Nature Communications, 8, 1774. https://doi.org/10.1038/s41467-017-01998-z
13. Jiang, B., Liang, Y., Xu, X., Zhang, J., Hu, M., & Shi, Q. (2014). Polycyclic aromatic hydrocarbons (PAHs) in ambient aerosols from Beijing: characterization of low volatile PAHs by positive-ion atmospheric pressure photoionization (APPI) coupled with fourier transform ion cyclotron resonance. Environmental Science & Technology, 48(9), 4716-4723. https://doi.org/10.1021/es405295p
14. Koch, B. P., & Dittmar, T. (2006). From mass to structure: an aromaticity index for high-resolution mass data of natural organic matter. Rapid Communications in Mass Spectrometry, 20(1), 926-932. https://doi.org/10.1002/rcm.7433
15. Liu, F., Luang, Y. Z., Zhu, R.L., Xiao, J., Xing, J. Q., Zhu, L. L., Ye, Q. T., Lv, Y. J., & Shi, Z. Q. (2025). Probing molecular level and subnanoscale stabilization mechanisms of organic carbon species during Fe(II)-induced ferrihydrite transformation. Environmental Science & Technology, 59(27), 13832-13843. https://doi.org/10.1021/acs.est.5c04803

16. Liu, F. H., Wang, Z. Q., Liu, J., Latif, J., Qin, J. J, Yang, H. Q., Jiang, W. J., Deng, Y. X., Yang, K. J., Ni, Z., Ding, Y. Y., Xie J., Wang, Y. H., & Jia, H. Z. (2024). Seasonal and spatial fluctuations of reactive oxygen species in riparian soils and their contributions on organic carbon mineralization. Environmental Science & Technology, 58(16), 7066–7077. https://doi.org/10.1021/acs.est.3c10756
17. Liu, J., Sheng, A. X., Li, X. X., Arai, Y. J., Ding, Y. F., Nie, M. J., Yan, M. Q., & Rosso, K. M. (2022). Understanding the importance of labile Fe(III) during Fe(II)-catalyzed transformation of metastable iron oxyhydroxides. Environmental Science & Technology 56(6), 3801-3811. https://doi.org/10.1021/acs.est.1c08044
18. Mikutta, C., Niegisch, M., Thompson, A., Behrens, R., Schnee, L. S., Hoppe, M., & Dohrmann, R. (2024). Redox cycling of straw-amended soil simultaneously increases iron oxide crystallinity and the content of highly disordered organo-iron(III) solids. Geochimica et Cosmochimica Acta, 371, 126–143. https://doi.org/10.1016/j.gca.2024.02.009
19. Murad, E. (1998). Clays and clay minerals: what can Mössbauer spectroscopy do to help understand them? Hyperfine Interactions. 117, 39-70.
20. Murad, E., & Wagner, U. (1994). Mössbauer study of pure illite and its firing products. Hyperfine Interactions. 91, 685-688.
21. Sheng, A. X., Liu, J., Li, X. X., Qafoku, O., Collins, R. N., Jones, A. M., Pearce, C. I., Wang, C. M., Ni, J. R., Lu, A. H., & Rosso, K. M. (2020). Labile Fe(III) from sorbed Fe(II) oxidation is the key intermediate in Fe(II)-catalyzed ferrihydrite transformation. Geochimica et Cosmochimica Acta, 272, 105-120. https://doi.org/10.1016/j.gca.2019.12.028
22. Sparks, D. L. (1996) Methods of soil analysis, Part 3: Chemical methods. Soil Science Society of America, Inc: Madison, Wisconsin, USA.
23. Thompson, A., Chadwick, O. A., Rancourt, D. G., & Chorover, J. (2006). Iron-oxide crystallinity increases during soil redox. Geochimica et Cosmochimica Acta, 70, 1710–1727. https://doi.org/10.1016/j.gca.2005.12.005
24. Thompson, A., Rancourt, D. G., Chadwick, O. A., Chorpver, J. (2011). Iron solid-phase differentiation along a redox gradient in basaltic soils. Geochimica et Cosmochimica Acta, 75, 119-133. https://doi.org/10.1016/j.gca.2010.10.005
25. Tomaszewski, E. J., Cronk, S. S., Gorski, C. A., & Ginder-Vogel, M. (2016). The role of dissolved Fe (II) concentration in the mineralogical evolution of Fe (hydr) oxides during redox cycling. Chemical Geology, 438, 163-170. https://doi.org/10.1016/j.chemgeo.2016.06.016
26. Winkler, P., Kaiser, K., Thompson, A., Kalbitz, K., Fiedler, S., Jahn, R. (2018). Contrasting evolution of iron phase composition in soils exposed to redox fluctuations. Geochimica et Cosmochimica Acta, 235, 89–102. https://doi.org/10.1016/j.gca.2018.05.019
27. Yang, L. J., Jia, B., Liu, J. B., Zhu, K. C., Qin, J. H., & Jia, H. Z. (2025). A novel perspective on the role of hydroxyl radicals in soil organic carbon mineralization within the detritusphere: stimulating C-degrading enzyme activities. Environmental Science & Technology, 59(10), 5045–5055. https://doi.org/10.1021/acs.est.4c13619

28. Yao, J. Y., Wang, H. W., Fang, J., Shan, S. D., Joseph, S. D., Van Zwieten, L., Zhu, K. C., Chen, D. J., & Jia, H. Z. (2025). Distribution hotspots, formation mechanisms, and ecological effects of reactive oxygen species in soil and sediment: a critical review. Environmental Science & Technology, 59(27), 13551–13565. https://doi.org/10.1021/acs.est.5c00581
29. Zhao, G. Q., Wu, B. B., Zheng, X. S., Chen, B. L., Kappler, A., & Chu, C. H. (2022). Tide-triggered production of reactive oxygen species in coastal soils. Environmental Science & Technology, 56, (16), 11888–11896. https://doi.org/10.1021/acs.est.2c03142
30. Zhou, Z., Latta, D.E., Noor, N., Thompson, A., Borch, T., & Scherer, M. M. (2018). Fe(II)-catalyzed transformation of organic matter–ferrihydrite coprecipitates: a closer look using Fe isotopes. Environmental Science & Technology, 52(19), 11142-11150. https://doi.org/10.1021/acs.est.8b03407
31. Zhu, Y., & Elzinga, E. J. (2014). Formation of layered Fe(II)-hydroxides during Fe(II) sorption onto clay and metal-oxide substrates. Environmental Science & Technology, 48(9), 4937-4945. https://doi.org/10.1021/es500579p

Tables

Table 1 Relative abundance (%) of the major biochemical classes of assigned formulas in DOC of soils at the end of 11 w anoxic incubation.

Soil	Lipids	Proteins	Carbohydrates	Unsaturated hydrocarbon	Lignin-like	Tannins	Condensed aromatics
DS	5.26	13.91	1.98	0.20	75.12	3.35	2.76
XT	3.95	9.85	0.46	0.06	79.14	3.94	4.77

Figures

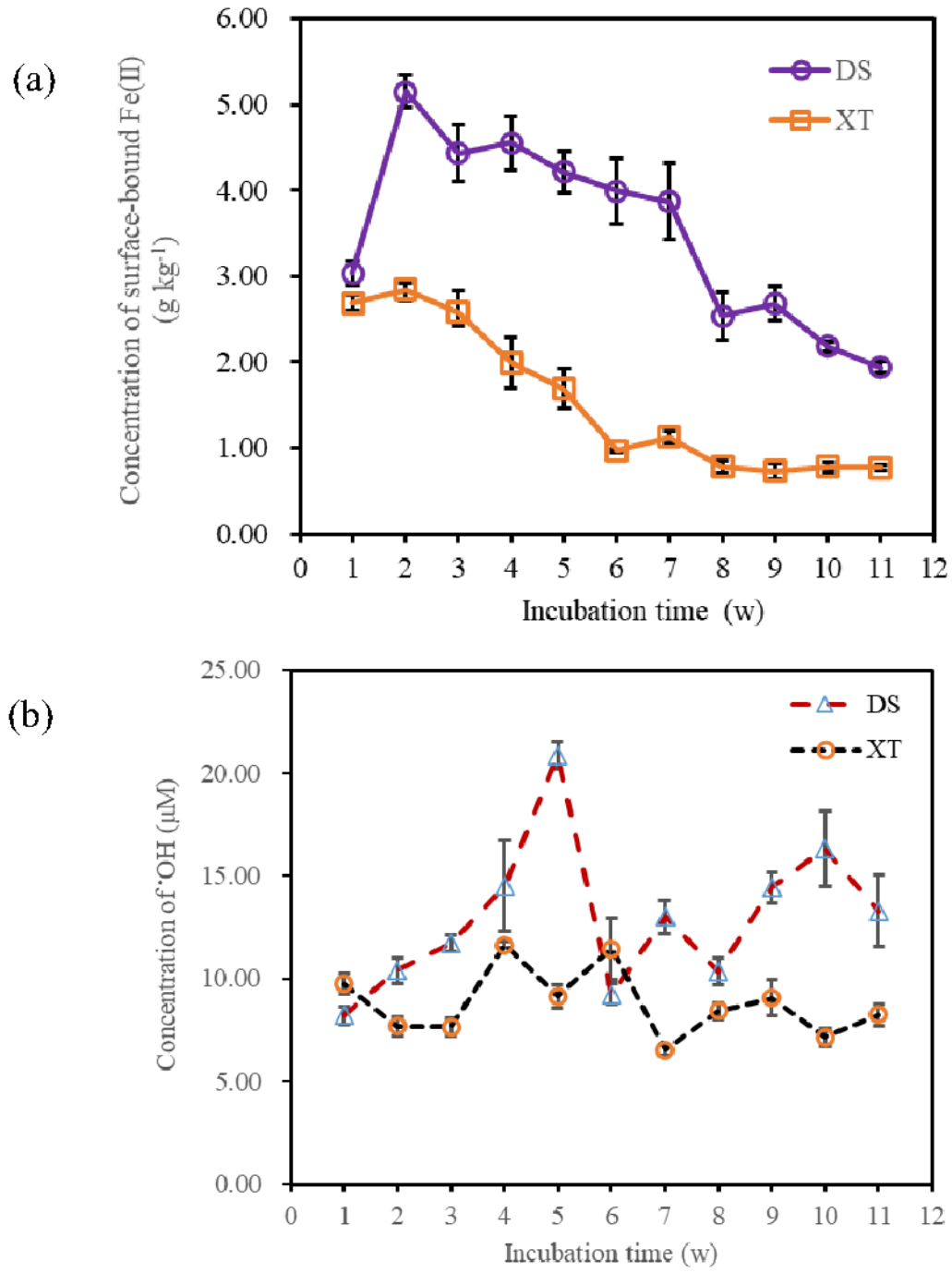


Figure 1

Redox fluctuation induced production of surface-bound Fe(II) (a) and ˙OH (b) during 11 w anoxic incubation.

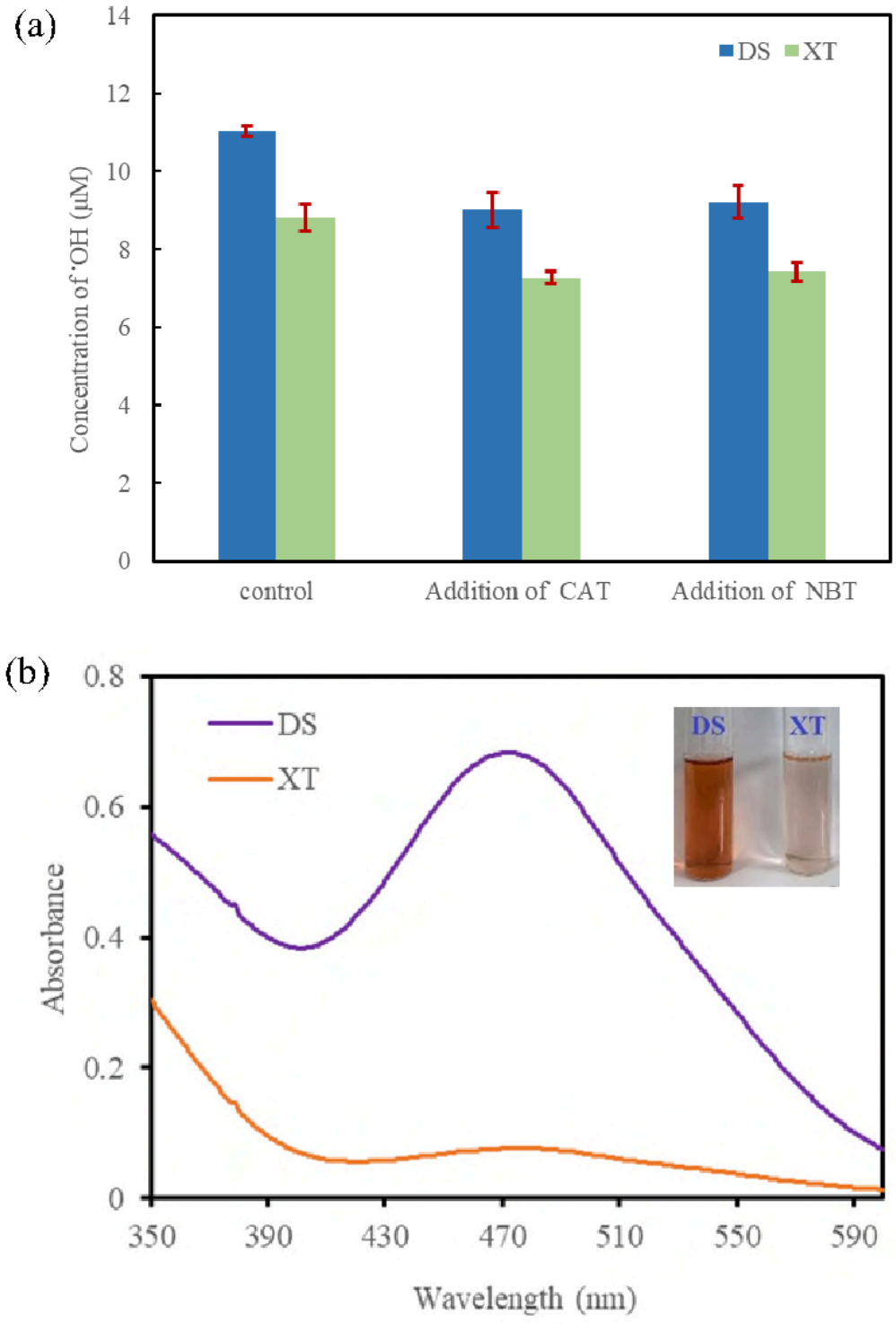


Figure 2

(a) Effect of scavengers, CAT (960 U ml^{-1}) and NBT (1.0 mM), on the production of ·OH in the DS and XT systems, (b) UV-vis absorption spectrum of XTT formazan, indication the formation of $O_2^{\bullet-}$, formed during the oxidation of Fe(II) in the DS and XT systems.

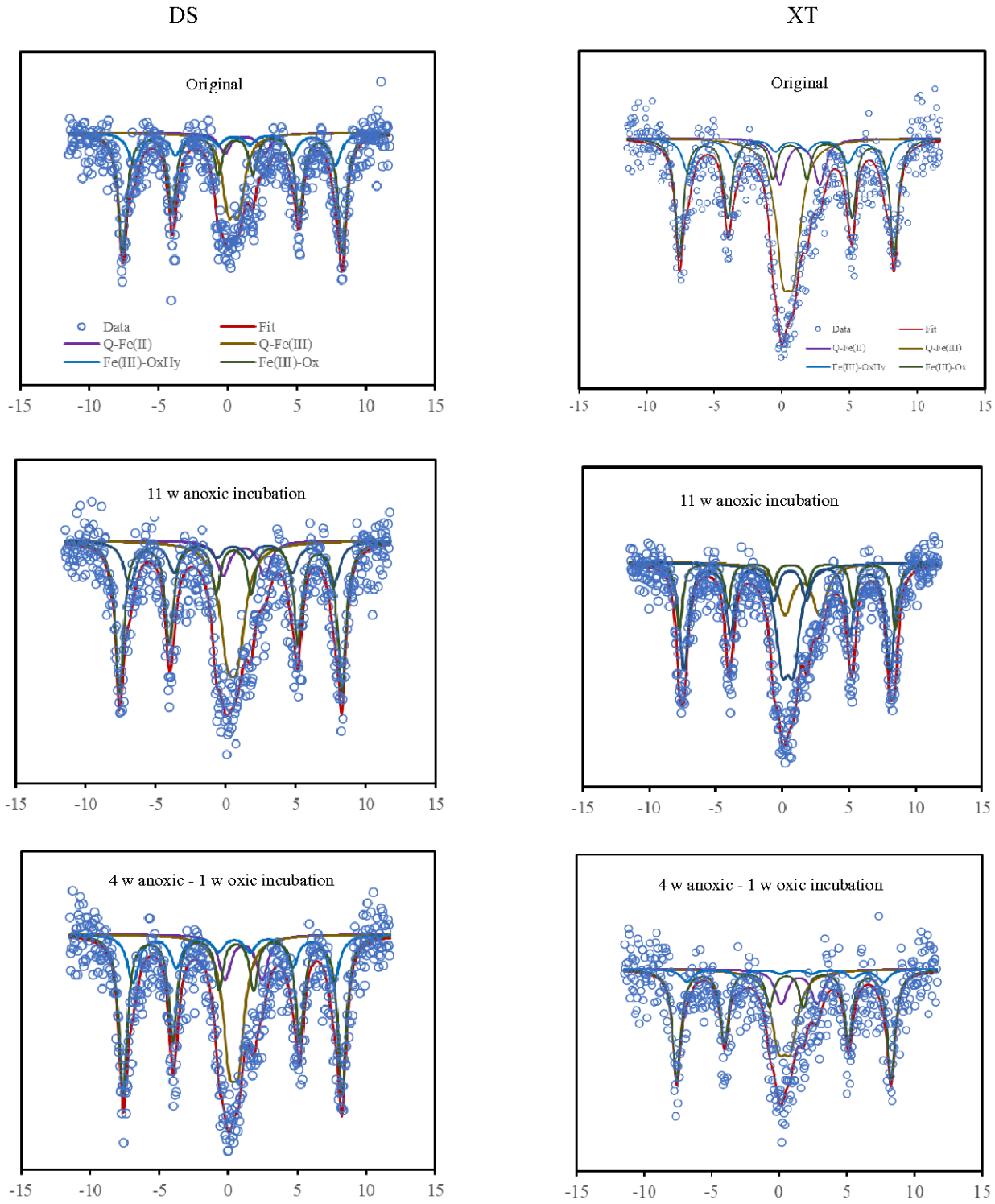


Figure 3

Fitted results for the abundance of iron phase components derived from the 6-k ^{57}Fe Mössbauer spectra. Q-Fe(II) = silicate bound Fe(II), Q-Fe(III) = organic/silicate bound Fe(III), Fe(III)-OxHy = Fe(III)-(oxy)hydroxides, Fe(III)-Ox = Fe(III)-oxides.

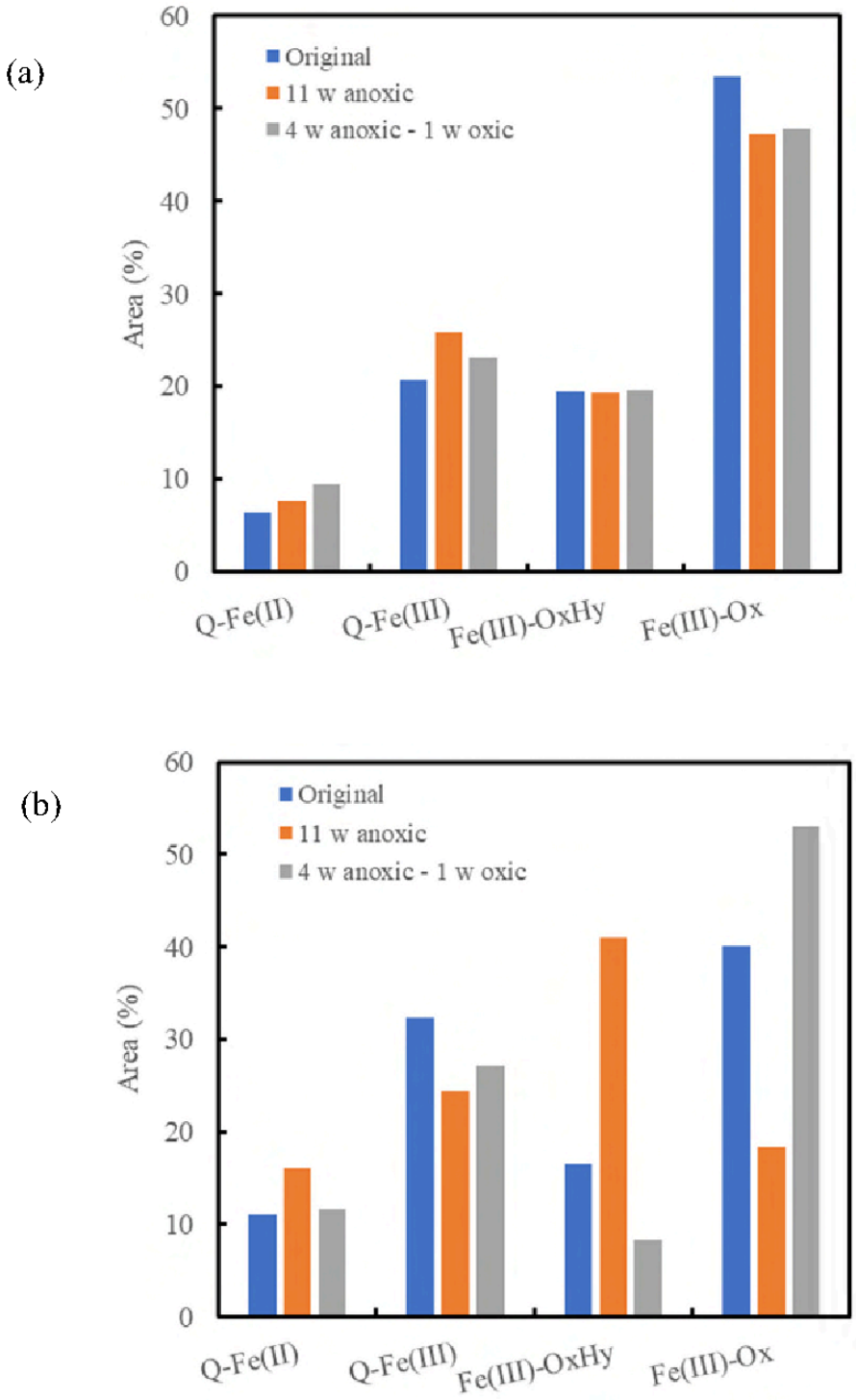


Figure 4

MBS results of DS (a) and XT (b) for the content percentage of iron phase components derived from the 6-k ^{57}Fe Mössbauer spectra. Q-Fe(II) = silicate bound Fe(II), Q-Fe(III) = organic/silicate bound Fe(III), Fe(III)-OxHy = Fe(III)-(oxy)hydroxides, Fe(III)-Ox = Fe(III)-oxides.

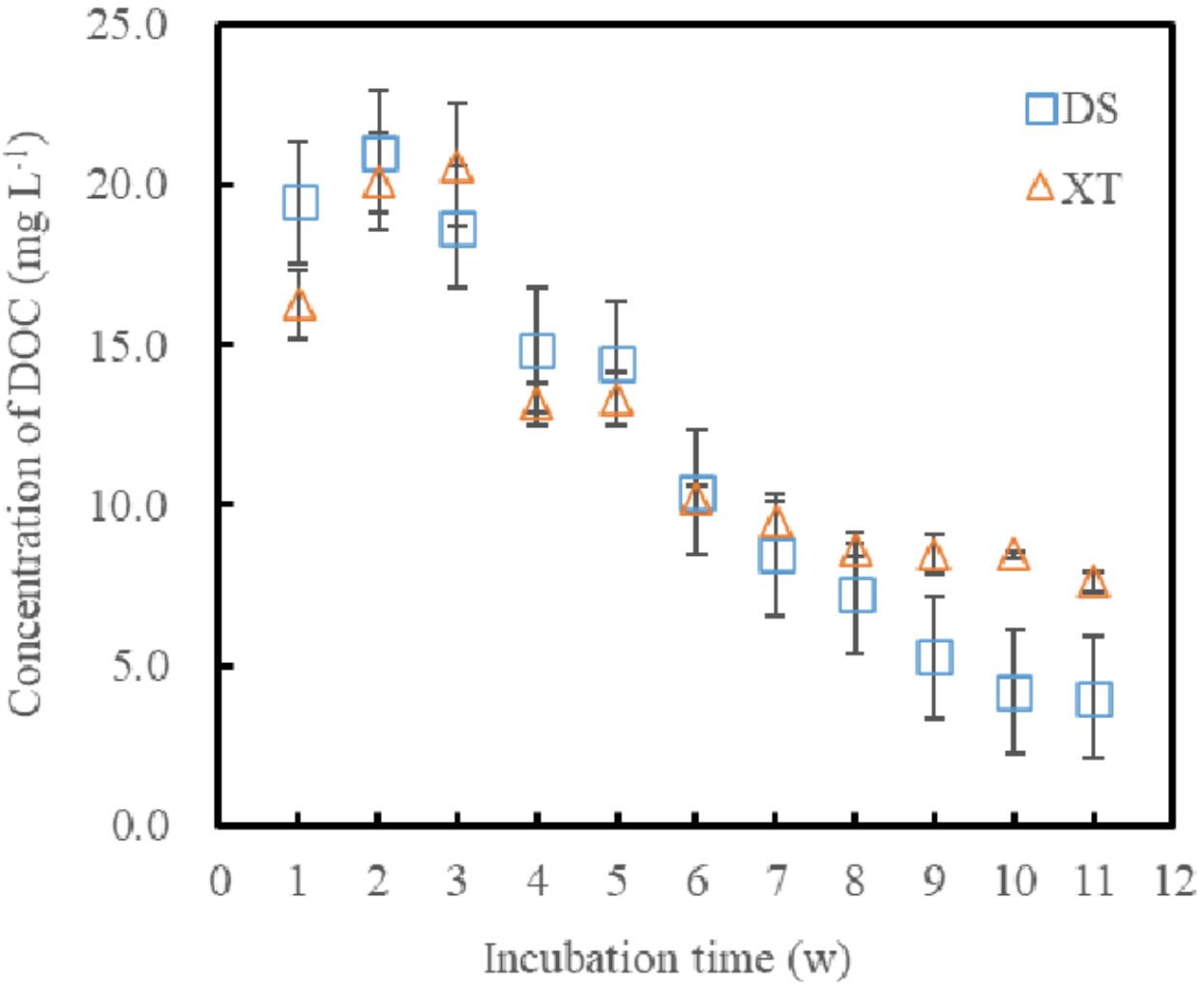


Figure 5

Release of SOC during the 11 w anoxic incubation.

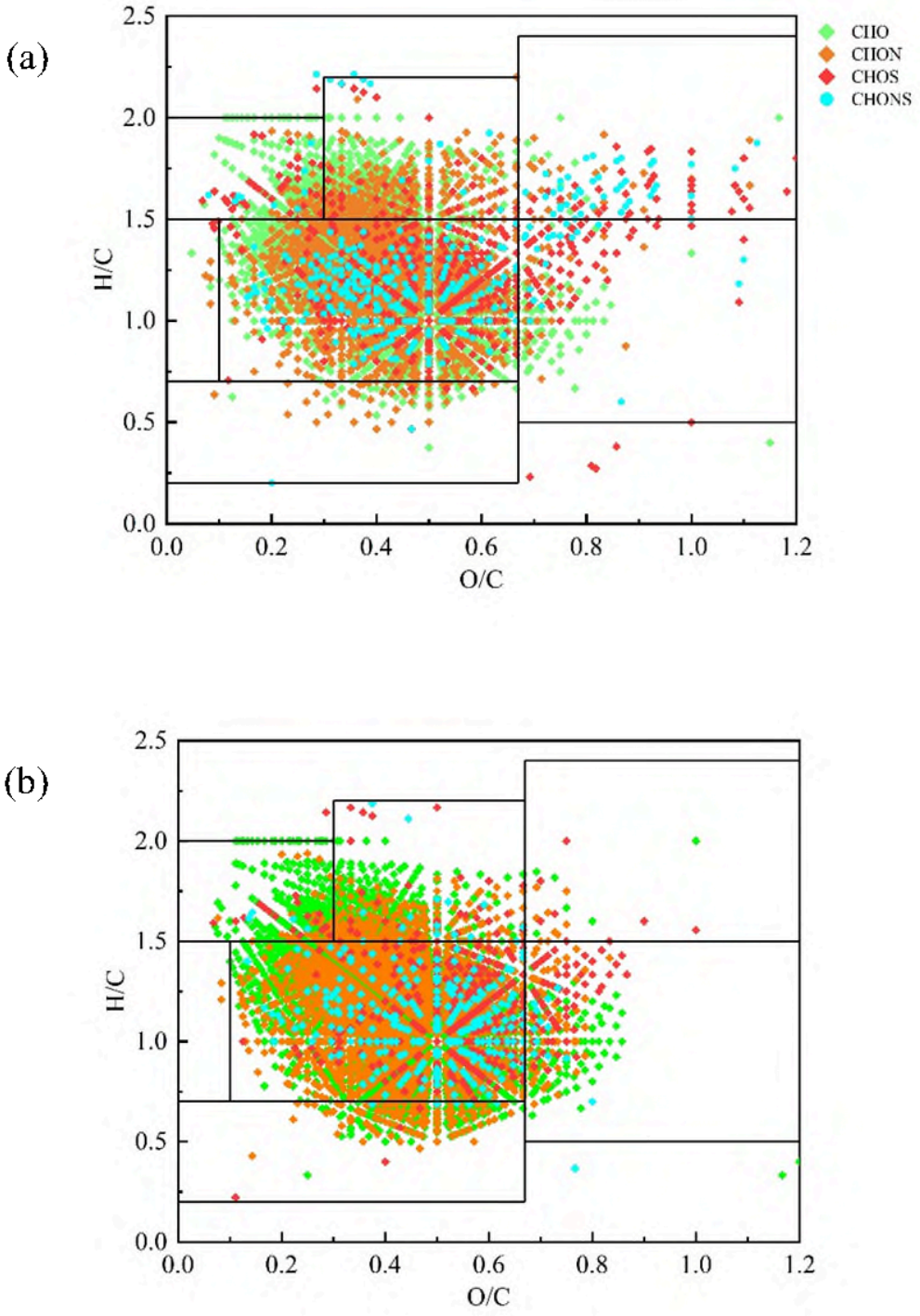


Figure 6

van Krevelen diagrams of assigned formulas of FT ICR-MS data in DOC of soils after 11 w anoxic incubation. (a) DS, (b) XT.

Supplementary Files

This is a list of supplementary files associated with this preprint. Click to download.

- Supplementarymaterials.docx